日本医放会誌：49（9），1152—1167，1989（平1）

Theoretical Analysis of Image Formation Process in Quantitative Dual-Energy Subtraction in a Single Exposure

Tsuguhisa Katoh
Department of Radiology and Radiation Research, Faculty of Dentistry,
Tokyo Medical and Dental University

Research Code No. : 208.1

Key Words : Bone mineral content, Dual-energy subtraction, Dichromatic X-rays, K-edge, Image formation

1回撮影による定量的エネルギー差分法の理論的解析

東京医科歯科大学歯学部歯科放射線学教室
加　藤　二　久

（平成元年2月14日受付）
（平成元年4月26日最終原稿受付）

K吸収端フィルタによって得られるquasidichromaticなX線を用いると，1回撮影によるエネルギー差分像から，被写体に含まれる骨ミネラル量や軟組織の厚さの定量が可能となる．この方法では低エネルギーX線吸収フィルタを挟んで2つの画像検出器を重ねて撮影し，管球側検出器で低エネルギーX線像を，後側検出器で高エネルギーX線像を得る．しかしこの場合，高エネルギーX線が管球側の画像に及ぼす影響が問題となる．本論文ではこの影響を補正する方法を，入射X線が完全にdichromaticであると仮定して理論的に導いた．更にこの仮定が成立する事の確認と補正に必要なパラメータを得るために，この撮影系の像形成過程を理論的に解析した．すなわち，増感紙蛍光体のエネルギー吸収が被写体の厚さに依って変化する様子をX線管が発生する連続スペクトルにフィルタと被写体による減弱率および蛍光体のエネルギー吸収効率を乗じた関数を積分して評価した．この結果，被写体に入射するX線はdichromaticと見做せる事を確認した．また補正に必要なパラメータを被写体と共に撮影する参照楔の陰影の解析から求める方法も，この結果から導き出された．理論計算と現実の撮影系との差異および補正の有効性をファントム実験で検証した結果，実験と計算は良い一致を示し，補正の有効性は被写体が厚い時に顕著に現われた．

1 Introduction

Dual energy subtraction technique has been utilized in clinical application[1)~4)] and has provided useful diagnostic information[5)6)]. The most application of this technique have, however, been limited only to enhance the soft tissue image, calcified lesion, contrast madia and others, while eliminating the image component of other tissue. Although the image is produced by a digital image processor, there is a tendency that the quantitativeness of the digital information has not been fully utilized for clinical diagnosis.

The beam hardening effect is one of the difficulties in the quantitative interpretation of the x-ray image produced by the conventional white x-rays. For this reason, the monochromatic beam such as

gamma-rays or characteristic x-rays has been used[7)~9)] when quantitative information is required. Since the current monochromatic source can not emit high intensity beam, therefore it requires a long time exposure to form an image. When a conventional x-ray generator with a K-dege filter such as tin is used, a high intensity quasi-monochromatic x-ray beam is obtained. In this case, the required tube load to produce an image (approximately 1000 mAs at FFD=1 m) is less than the maximum acceptable load of an ordinary diagnostic generator, and the logarithm of the transmitted x-ray intensity is precisely proportional to the object thickness[10)].

In the dual-energy subtraction technique, the artifact caused by the motion of the object is another important problem. In order to overcome the problem, a method with a single exposure was devised[11)~14)]. In this method, two image receptors are stacked and a filter is inserted between them to absorb the low energy x-rays. The image of the receptor in tube side is formed mainly by the lower energy x-rays and that in the back side is produced by the higher energy x-rays.

Using quasi-dichromatic x-rays obtained by a tin K-edge filter, 1 have developed a method for dual-energy subtraction in a single exposure[11)]. This method could measure the bone mineral content accurately when the object was thoroughly thin. For the thick object, the attenuaiton of the higher energy x-rays was much less than that of the lower energy x-rays, so the contribution of the higher energy x-rays to the tube side image could not be neglected. This contribution caused a systematic error in the resultant quantitative image data.

In this study, the image formation process in the dual-energy subtraction by a single exposure was theoretically analyzed. In addition, a method to correct the effect of the high energy x-rays on the image by lower energy x-rays was developed. Further, the accuracy of the theoretical analysis and the efficiency of the correction for the thick object was tested by the phantom experiment.

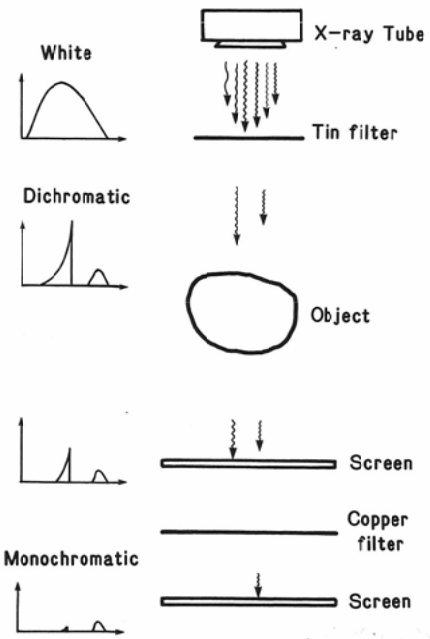

Fig. 1　A schematic illustration of the radiographing system used for the dual-energy subtraction in a single exposure.

2 Theoretica analysis

2-1 The radiographing system

The radiographing system as outlined in Fig. 1 was described in details in my previous paper[11]. Briefly, the x-ray beam was dichromized by 0.3 mm tin filter. In the cassette, a low speed film-screen system, a 0.8 mm thick copper filter to absorb the lower energy x-rays and a high speed film-screen system were piled up one upon another. The image on the tube side film was formed mainly by the x-rays in the spectral peak at the energy just below the K-absorption edge, and that on the back side film was produced by the x-rays in the higher energy peak close to the tube potential.

Two wedges were mounted on the object plane together with the object. One was made of epoxy resin and bone mineral equivalent material (a mixture[15] of $Ca_3(PO_4)_2$ 3 mol and $CaCO_3$ 1 mol, whose atomic composition was very close to that of hydroxyapatite $Ca_{10}(PO_4)_6(OH)_2$). This wedge was used to correct the fluctuations of the x-ray intensity and the film processing condition for each radiogram. It is called "reference wedge" in this paper. Another wedge was made of 100% epoxy resin and used to determine the weighting factor for the subtraction.

2-2 First approximation of the image formation process

In the first approximation, following assumptions are made.

1) The tube side image is formed by the lower energy (E_1) monochromatic x-rays alone.
2) The back side image is formed by the higher energy (E_2) monochromatic x-rays alone.
3) The incident x-ray intensity I_0 and the response of the image receptor (H-D curve of the film-screen system) are homogeneous over the image.
4) The epoxy resin is the soft tissue equivalent material.

The basic mathematical concept of the dual energy subtraction is the simultaneous equations as,

$$\exp\{-U_bX_b - U_sX_s\}=(I/I_0) \tag{1-1}$$

$$\exp\{-U_b^*X_b - U_s^*X_s\}=(I/I_0)^* \tag{1-2}$$

where U_b and U_s are mass attenuation coefficients (cm^2/g) of bone mineral and soft tissue, respectively, for energy E_1, and X_b and X_s are corresponding products (g/cm^2) of their thickness and specific density. I/I_0 is the x-ray attenuation by the object through the attenuation path from the focus to the pixel of interest P. The symbols with asterisk denote the quantities for energy E_2. The quantites in the right side of the equations are to be measured from the image. The solutions of X_b and X_s are the pixel data of the resultant bone mineral image and the soft tissue image, respectively, by the dual energy subtraction.

The reference wedge is used to correct the fluctuations of the x-ray intensity and the working condition of the image receptor (film processing condition). Based on the assumption 3), the reference wedge thickness X_r that present the same gray level (film density) to that of the pixel P is the measure of the x-ray attenuation I/I_0.

$$I/I_0=\exp\{-U_rX_r\} \tag{2}$$

Where U_r is the mass attenuation coefficient of the reference wedge. Then equations (1-1) and (1-2) are rewritten as,

$$(U_b/U_r)X_b + (U_s/U_r)X_s = X_r \tag{3-1}$$

$$(U_b^*/U_r^*)X_b + (U_s^*/U_r^*)X_s = X_r^* \tag{3-2}$$

X_r and X_r^* are called "reference material equivalent thickness (RMET)" at energy E_1 and E_2, respectively, in this paper.

Using this expressions, we need merely the ratios of the mass attenuation coefficients. The ratio U_s/U_r is determined from the RMET of 100% epoxy resin wedge.

$$\exp\{-U_{ep}X_{ep}\}=\exp\{-U_rX_r\}$$
$$\therefore U_{ep}/U_r=X_r/X_{ep} \quad (4)$$

where U_{ep} and X_{ep} are the mass attenuation coefficient and the thickness of the epoxy wedge. By assumption 4), U_s/U_r is equal to U_{ep}/U_r. The ratio U_b/U_r is calculated from the value of U_{ep}/U_r by Eq. (6) based on Eq. (5).

$$U_r=P_bU_b+P_{ep}U_{ep} \quad (5)$$
$$U_b/U_r=\{1-P_{ep}(U_{ep}/U_r)\}/P_b \quad (6)$$

where P_b and P_{ep} are the weight fractions of the bone mineral equivalent material and the epoxy resin in the reference wedge, respectively. U_b^*/U_r^* and U_{ep}^*/U_r^* are also determined in the same way.

2-3 Approximation of image formation by dichromatic x-ray attenuation model

In the next step of the approximation, assumption 1) is modified as,

1') The tube side image is formed by the dichromatic incident x-rays (photon energy E_1 and E_2).

Then Eq. (1-1) is rewritten as

$$Q\exp\{-U_bX_b-U_sX_s\}+Q^*\exp\{-U_b^*X_b-U_s^*X_s\}=Q\exp\{-U_rX_r\}+Q^*\exp\{-U_r^*X_r\} \quad (7)$$
$$(Q+Q^*=1)$$

where Q and Q* are the intensity fractions of the low energy and the high energy x-ray components in the incident x-rays.

Substituting Eq. (3-2) to the exponent of the second term in the left side of Eq. (7), Eq. (8) is derived.

$$(U_b/U_r)X_b+(U_s/U_r)X_s=$$
$$X_r-(1/U_r)\log_{e(sufix)}[1+(Q^*/Q)\exp\{U_rX_r\}(\exp\{-U_r^*X_r\}-\exp\{-U_r^*X_r^*\})] \quad (8)$$

Comparing Eq. (8) with Eq. (3-1), we can regard the logari thmic trem in the right side as the correction term for the contribution of the high energy component. For the correction, values for Q^*/Q, U_r and U_r^* are required. These can be determined using the results of the following simulation.

3 Simulation of the image formation process

The purposes of the simulation were to confirm that assumptions 1'), 2) and 4) are realized in the acutual radiographing system and to determine the parameters required for the correction.

3-1 Method

3-1-1 Mathematical model

For this purpose, the absorbed energy D by the screen is the essential quantity. It is calculated by Eq. (9).

$$D=\int\Phi(E)Ea(E)\exp(-F(E)-\mu_o(E)t_o)dE \quad (9)$$
$$F(E)=\mu_{Al}(E)t_{Al}+\mu_{Sn}(E)t_{Sn}+\mu_{Cu}(E)t_{Cu}+\mu_p(E)t_p$$

where $\Phi(E)$ is the spectrum from the X-ray tube, Ea(E) is the energy absorbed locally by the phosphor per incident photon of energy E, F(E) is the filtration that is taken into account in the simulation, and μ and t are the attenuation coefficient and thickness. The subscripts o, Al, Sn, Cu and p are the materials of object, aluminum, tin, copper and phosphor of the tube side screen, respectively. The t_{Cu} and t_p are zero for the tube side image. The t_{Al} is the aluminum equivalent thickness of the total filtration excluding the tin, copper and the tube side screen phosphor. The attenuation by the film and the screen base were neglected.

Because the objects were separated by 20 cm from the cassette, the effects of the scattered x-rays could be considered homogeneous over the image. They were, therefore, automatically corrected in RMET determination. For this reason, the scattered x-rays were neglected in the calculation.

In this simulation, photon cross sections compiled by Storm et al.[16] and reconstructed to floppy disk files for personal computers by Harata et al.[17] were used.

3-1-2 X-ray spectra

It was assumed that the target angle was 17° and that the inherent filtration of the x-ray tube was 1.5 mmAl.

The white x-ray spectra at the constant tube potential from 30 to 70 kV were taken from the catalogue data by Birch et al.[18] By means of the linear interpolation, spectra at every 1 kV tube potential were prepared. The spectra at the tube potential from 18 to 29 kV were estimated by Kramers'[19] theory.

The spectra for the tube potential wave form of 3-phase 6-peak and single phase 2-peak from 49 to 61 kVp were estimated by summation of weighted constant potential spectra. The wave form were assumed to be sinusoidal and its superimposition. The x-ray generation at the tube potential below 18 kV was neglected.

The aluminum filtration was varied from 1.5 to 2.3 mm.

3-1-3 Attenuation by the object

For the object materials, bone mineral equivalent material, epoxy resin, mixture of them (P_b=38.4%, 47.8% and 69.1%) and water were chosen. The atomic composition of epoxy resin was assumed to be C:H:O:N=66:96:9:4.

In order to check the accuracy of the transmitted spectra, spectral measurements were carried out using a germanium detector (GLP-10180/07: EG & G Ortec, Oak Ridge, Tennessee) and a constant potential generator (PW1732: Philips, Alemlo, the Netherlands). The focus-detector distance was 1.2 m and the beam was collimated into 2 mm in diameter at the detector window. As the object, the bone phantom wedge (69.1% bone mineral equivalent material and epoxy resin) and the pure epoxy resin wedge were mounted at 20 cm apart from the detector. The spectra measured for various tube potential form 51 to 59 kV and for various object thickness were compared with the calculated spectra. They agreed within the variaiton of ± 5% with each other. Fig. 2 shows examples of the comparison.

3-1-4 Energy absorption by screen phosphor

The Ea(E) in Eq. (9) was calculated according to Birch et al[18]. The assumed composition and thickness of the phosphor were Gd_2O_2S: 31.7 mg/cm² for the tube side screen (Min-R: Kodak, Rochester, New York) and LaOBr: 96.5 mg/cm² for the back side screen (Quanta III: Dupont, Wilmington, Delaware).

Fig. 3 shows examples of the calculated enegy absorption spectra by the screen phosphors. The

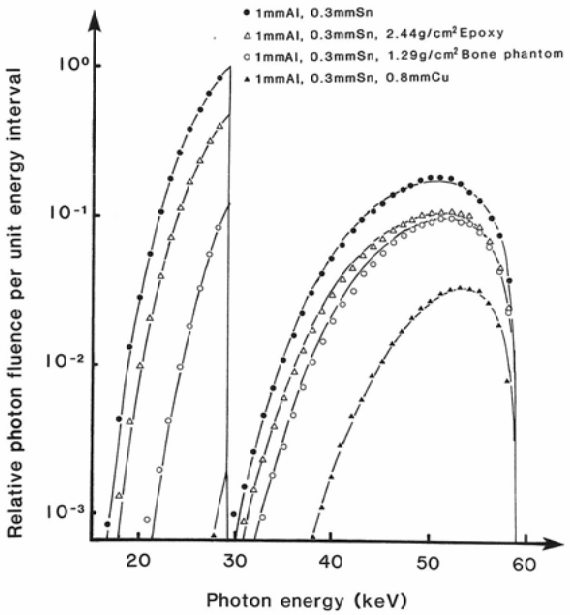

Fig. 2 The examples of the comparison between the simulation and the spectral measurement. The tube potential was 59 kVcp and the filtration was 1.0 mmAl and 0.3 mmSn. The measured x-ray spectra were shown for the output x-rays (●), the transmitted x-rays through the 2.44 g/cm² thick epoxy resin wedge (△), the 1.29 g/cm² thick bone phantom comtaining 69.1% bone mineral equivalent material (○) and the 0.8 mm thick copper filter (▲). The solid lines were derived from the simulation.

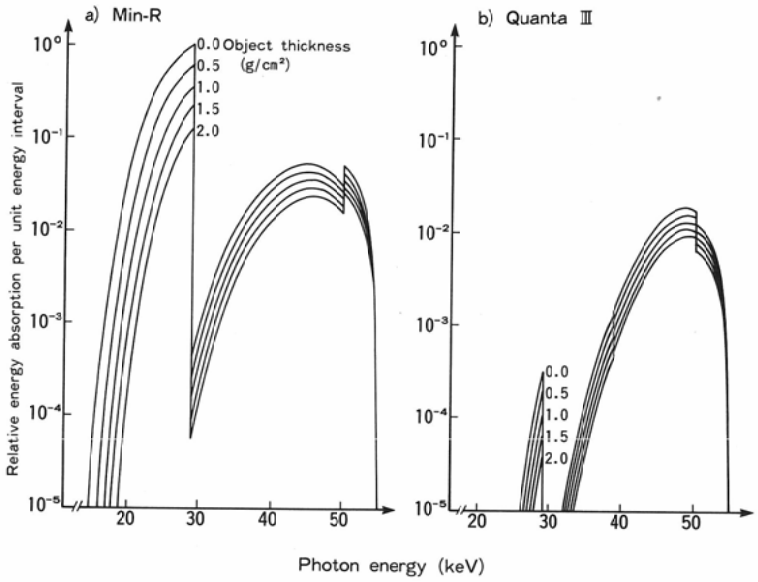

Fig. 3　The examples of the simulated spectra of energy absorption in the screen phosphor. Tube potential was 55 kVp with 3-phase 6-pulse wave form. Filtrations of 1.5 mmAl inherent to x-ray tube, 0.3 mmSn and 0.8 mmCu between the two screens were used in the simulation. Bone phantom containing 38.4% bone mineral equivalent material was used as an object. a) The tube side screen Min-R b) The back side screen Quanta III.

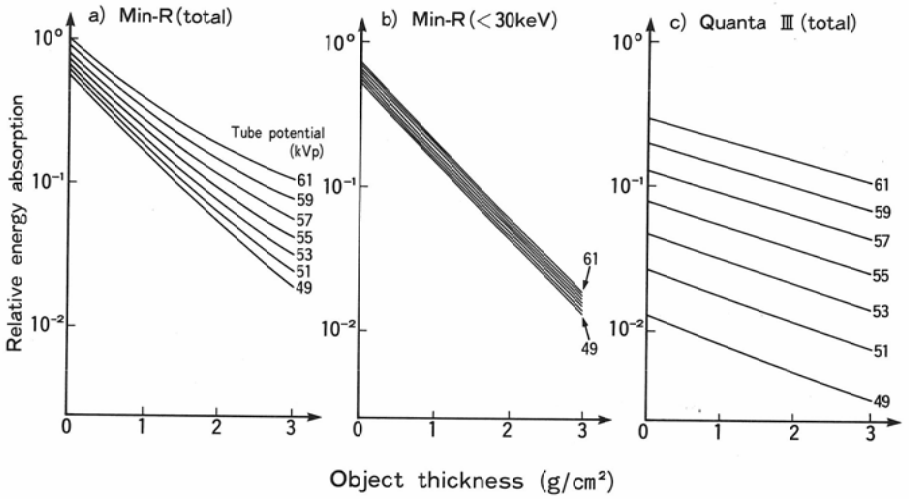

Fig. 4　The relative transmission through the object measured as the absorbed energy in the screen phosphor was plotted against the object thickness. The filtration and the object were the same as in Fig. 3.
a) The tube side screen (Total). b) The tube side screen (Low energy component). c) The back side screen (Total).

integrated values of the spectra for various object thickness gave the attenuation curve of the x-rays, measured as the energy absorption in the screen phosphors (Fig. 4a and 4c). The integration below 30 keV gave the attenuation of the lower energy component x-rays forming the tube side image (Fig. 4b).

3-1-5 Attenuation coefficients and dichromatic attenuation model

From the simulated attenuation data of the lower enegy component x-rays absorbed by the tube side screen phosphor (Fig. 4b) and all the x-rays absorbed by the back side screen phosphor (Fig. 4c), the mean attenuation coefficients of the object materials were calculated by the least squares method.

In accordance with assumption 1'), the simulated attenuation curves of all the x-rays absorbed by the tube side screen phosphor (Fig. 4a) were approximated as the sum of the two components. Using the mean attenuation coefficients calculated above, the best fit fraction of either components Q and Q* in Eq. (7) were found by the least squares method.

The simulation was carried out for the tin filter from 0.29 to 0.31 mm and the copper filter from 0.79 to 0.81 mm to determine the effect of variation in the filter thickness.

3-2 Results

3-2-1 Attenuation coefficients

The simulated attenuation curves of the low energy component x-rays absorbed by the tube side screen phosphor (Fig. 4b) and the x-rays absorbed by the back side screen phosphor (Fig. 4c) were linear in the semi-logarithmic plot. These x-rays could be regarded, therefore, as monochrome. This result justified the assumption 2) in the approximation.

Attenuation coefficients for the low energy component x-rays calculated by the least squares fitting to the simulated attenuation data were listed in Tab. 1. They did not significantly vary with the tube potential, its wave form and filtration. The ranges of variation were within 2%. For the ratios U_b/U_{ep} and U_s/U_{ep}, the ranges of variation were less than 0.7%.

The attenuation coefficients for the high energy component x-rays varied with the tube potential, its wave form and the aluminum filtration. The variation for each material, however, was expressed by a unique linear function of the ratio $r=U_b^*/U_{ep}^*$ as shown in Fig. 5. These were fitted as

$$U_b^* = 0.2622r - 0.1604 \quad (|Er|_{max}=.006) \tag{10}$$

$$U_{ep}^* = 0.01702r + 0.15726 \quad (|Er|_{max}=.0002) \tag{11}$$

$$U_s^*/U_{ep}^* = 0.0466r + 0.9787 \quad (|Er|_{max}=.001) \tag{12}$$

where, $|Er|_{max}$ were the maximum absolute value of the fitting errors in the range of r from 2.6 to 3.6. These errors remain less than the range of variation of the attenuation coefficients to the low energy x-rays.

Using the method described in Section 2-2, we can measure $r=(U_b^*/U_r^*)/(U_{ep}^*/U_r^*)$ from the wedge

Table 1 The mass attenuation coefficients of the object material to the lower energy (<30keV) component x-rays absorbed by the tube side screen (Min-R).

Wave form peak	Tube potential kV (p)	Aluminum filter mm	Atten. coeff. cm²/g			Ratio	
			Bone mineral (U_b)	Epoxy resin (U_{ep})	Water (U_s)	(U_b/U_{ep})	(U_s/U_{ep})
2	49	1.5	2.626	.3209	.4397	8.183	1.370
2	55	1.5	2.615	.3200	.4383	8.172	1.370
2	61	1.5	2.606	.3194	.4371	8.164	1.369
2	61	2.3	2.580	.3168	.4333	8.145	1.368
6	49	1.5	2.608	.3194	.4372	8.165	1.369
6	55	1.5	2.600	.3187	.4360	8.157	1.368
6	61	1.5	2.594	.3183	.4353	8.151	1.368
6	61	2.3	2.568	.3158	.4317	8.132	1.367
CP	55	1.5	2.597	.3185	.4357	8.154	1.368
CP	61	2.3	2.566	.3156	.4314	8.130	1.367

CP ; Constant potential

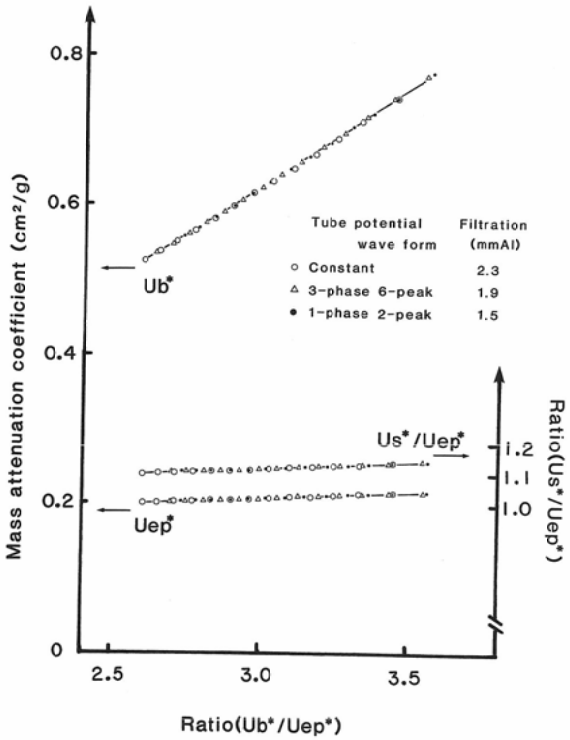

Fig. 5 The mass attenuation coefficients of the object materials to the higher energy component x-rays.
U_b^* and U_{ep}^* denote the mass attenuation coefficient of the bone mineral and the epoxy resin, respectively. U_s^*/U_{ep}^* denotes the ratio of the mass attenuation coefficient of water to that of the epoxy resin.
U_b^*, U_{ep}^* and U_s^*/U_{ep}^* varied with the tube potential, its wave form and the aluminum filtration, nevertheless, their variations were expressed as the unique function of the ratio U_b^*/U_{ep}^* for each material.

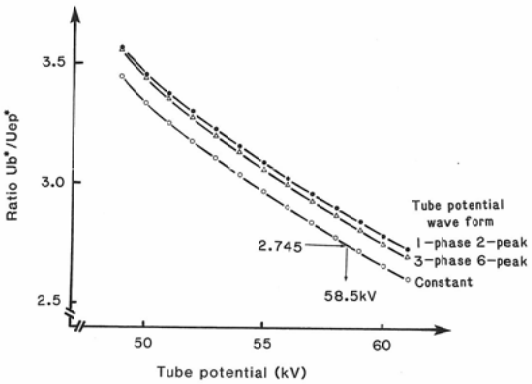

Fig. 6 The variation of the ratio U_b^*/U_{ep}^* with the tube potential and wave form.
There was no dependency on the aluminum filtration.

images on the back side film. Fig. 6 shows the variation of r with the tube potential. The variation of r with aluminum filtration was within a ± 0.13% range. We can thus regard r as an index of the tube potential.

Since the values for U_s/U_{ep} and U_s^*/U_{ep}^* were not unity, assumption 4) could not be justified. For the attenuation coefficient of the soft tissue, we must multiply the correction factors U_s/U_{ep} or U_s^*/U_{ep}^* to that of epoxy resin.

3-2-2 Dichromatic attenuation model

The attenuation curves of all the x-rays absorbed by the tube side screen phosphor (Fig. 4a) suggested that assumption 1), which assumed that the tube side image was formed by the monochromatic x-rays, could not be justified, because the gradients of the curves was reduced with the increase of the object thickness. Fig. 7 illustrated the dichromatic approximation of the attenuation data of the tube side screen energy absorption. For all the spectrum calculated in this work, the attenuation curves were well approximated within ± 3% error. Then we can consider that assumption 1') was justified.

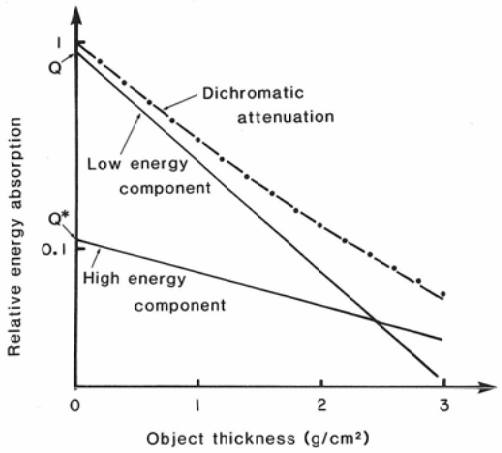

Fig. 7 An example of the attenuation curve fitting based on the dichromatic attenuation model for the tube side screen.
The closed circles indicate the attenuation data by the simulation. The solid lines indicate the attenuation curves of the two monochromatic x-rays and that of the sum of them.

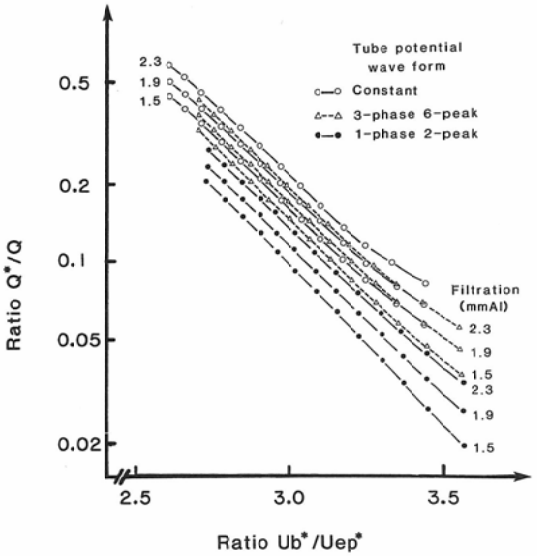

Fig. 8 The intensity ratio of the high energy component x-rays and the low energy component x-rays Q*/Q as the function of the ratio $r=U_b^*/U_{ep}^*$.
The points indicate the simulated value at every 1 kV tube potential. The curves indicate the fitted values by Eq. (13).

The ratio of the fraction of the high energy component to that of low energy Q*/Q depended on the tube potential, its wave form and the aluminum filtration, as shown in Fig. 8. For each wave form and filtration, the variation of Q*/Q with the tube potential were well fitted by polynomial of r as,

$$\log(Q^*/Q)=C_0+C_1r+C_2r^2+C_3r^3 \tag{13}$$

where C_0, C_1, C_2 and C_3 were fitting parameters. The fitting error was 1.3% at maximum for all the calculated spectra.

The variation with the added filter thickness approximately obeyed the exponential law, that was written as

$$Q^*/Q=K\exp[\{\mu_{Al}(\bar{E}_1)-\mu_{Al}(\bar{E}_2)\}t_{Al}] \tag{14}$$

where K was a constant, and $\bar{E}_1$ and $\bar{E}_2$ were the effective energy of each component, respectively. The $\bar{E}_1$ was expected to be constrant because its main determining factor was the K-edge energy. The $\bar{E}_2$ seemed to vary with the tube potential, its wave form and the total filtration like a white x-ray beam. The variation of $\mu_{Al}(\bar{E}_2)$ with the aluminum filtration thickness t_{Al} was small because the tin filter was dominant in the total filtration.

3-2-3 Error due to tin and copper filter thickness

In the low energy component region (20 to 30 keV), the ratio of linear attenuation coefficient of tin to that of aluminum are 33 (the range of variation is ± 1). From this value, we can estimate the error propagation to U_b, U_{ep} and U_s/U_{ep} due to the error of the nominal thickness of the tin filter. A 10 μm thick tin filter is equivalent to a 0.33 mm thick aluminum filter. Using the values for 1.5 and 2.3 mm aluminum filtration in Tab. 1, the quota allotment estimated the error propagation to be less than 0.1% in ratio U_b/U_{ep} and U_s/U_{ep}, and to be less than 0.6% in U_b and U_{ep}.

Simulations for 0.30 ± 0.01 mm tin filter and for 0.8 ± 0.01 mm copper filter gave the error estimation

for the high energy x-rays. The resulted U_b*, U_{ep}* and U_s*/U_{ep}* versus r did not vary more than ± 0.15%, which was the same order as the fitting precision of equations (10), (11) and (12). The maximum deviation in Q*/Q from Eq. (13) was 5.3%. This range of deviation was acceptable because it was used only in the small correction term.

From these estimated error propagation, we could consider that all the parameter used in the subtraction process was not afected by the variation in the thickness of about 10 μm of the tin and the copper filter.

4 Application

4-1 Advanced algoithm for quantitative energy subtraction

The dual energy subtraction algorithm used in my previous paper[11] was based on the first approximation. Present simulation made it clear that the high energy x-ray contribution in the tube side image formation must be corrected and that the contribution could be estimated from the ratio r=U_b*/U_{ep}*, which could be measured from the image.

Because the high energy x-ray contribution varied with the tube potential, and because the tube potential fluctuated for each radiogram, we were obliged, in the old method, to measure the mass attenuation coefficient ratios in Eq. (3-1) from the image for each radiogram. The measurement led an additional error. The result of the simulation confirmed that the attenuation coefficients of the object materials to the low energy component x-rays was independent of the tube potential, and that we could determine, in advance, their accurate values.

Based on these results, a new dual energy subtraction algorithm was derived.

4-1-1 Coefficients in the simultaneous equations

In the new algorithm, we solved the simultaneous equations (8) and (3-2).

The ratios U_b/U_r and U_{ep}/U_r in the left side of Eq. (8) were determined from the weight fraction of the bone mineral equivalent material in the reference wedge based on Eq. (5) as,

$$U_b/U_r=1/\{P_b + P_{ep}(U_{ep}/U_b)\} \quad (15\text{-}1)$$

$$U_s/U_r=(U_s/U_{ep})/\{P_b(U_b/U_{ep}) + P_{ep}\} \quad (15\text{-}2)$$

From Tab. 1, the value for U_b/U_{ep} was decided to be 8.172 for 2-peak wave form, 8.157 for 6-peak and 8.142 for constant potential. The value of U_s/U_{ep} was regarded as a constant of 1.369 for any tube potential wave form.

The ratios U_{ep}*/U_r*, U_b*/U_r* and r were measured from the the image of the back side film. Using r and Eq. (12), U_s*/U_{ep}* was determined. It was multiplied by U_{ep}*/U_r* to determine U_s*/U_r*.

4-1-2 Correction for the effect of the high energy x-rays

The values for U_r, U_r* and Q*/Q were required to determine the correction term in Eq. (8).

The value for U_r was determined by Eq. (5) using U_b=2.60 cm^2/g and U_{ep}=0.310 cm^2/g from Tab. 1, and U_r* was also determined by Eq. (5) using U_b* and U_{ep}*, which were calculated by Eq. (10) and Eq. (11).

Q*/Q was determined by Eq. (13). The parameters C_0, C_1, C_2 and C_3 were prepared for each wave form and aluminum filtration in 0.2 mm steps. For the fine adjustment of the aluminum filtration less than 0.2 mm, Eq. (14) was used by the interpolation.

4-2 Experiment

In oder to check the accuracy of the simulation and efficiency of the correction, a phantom experiment was carried out.

4-2-1 Material and method

The phatoms were made of a mixture of epoxy resin and bone mineral equivalent material in varied content. They were cut into straight sloping surface and the parametors were characterized in Tab. 2.

The phantoms were radiographed by a constant potential x-ray generator (HF-100: Pantak, Birkshire, England), whose inherent filtration was 1.0 mm thick beryllium and the added filtration was 1.5 mm thick aluminum. Focus-object distance and focus-film distance were 1.0 m and 1.2 m, respectively. The tube potential, tube current and exposure time were 58.0 kV, 50.0 mA and 20s, respectively, in nominal value on the controller. For the film-screen systems, Min-R/MR1 (Kodak) and Quanta III/Cronex 6 (Dupont) were used. The film was manually processed by Hi-Rendol (Fuji Photo Film, Tokyo, Japan) for 4 min at 20°C. The film density was measured by a micro-densitometer (Model 2405: Abe Sekkei, Tokyo, Japan). The measuring apertue was 0.2 mm × 2.0 mm.

4-2-2 Results

Fig. 9 shows the comparison of RMETs by the experiment to those by the simulation. The closed circles indicate the RMETs measured by the experiment and the solid lines, those predicted by the simulation. The open circles indicate the values after the correction for the high energy x-ray contribution by the advanced algoithm, and the broken lines the predicted RMETs by the simulation, in which the image was assumed to be formed by the low energy x-rays alone. These experimental values agreed with

Table 2 Phantoms used in the experiment.

Wedges	Content (%)		Density (g/cm^3)	Height (mm)	Length (mm)
	Mineral	Epoxy			
Reference	47.8	52.2	1.615	15.1	55.0
Pure epoxy	—	100.0	1.121	41.8	65.2
Sample	38.4	61.6	1.482	15.2	54.9

All phantoms are straight sloping wedges.

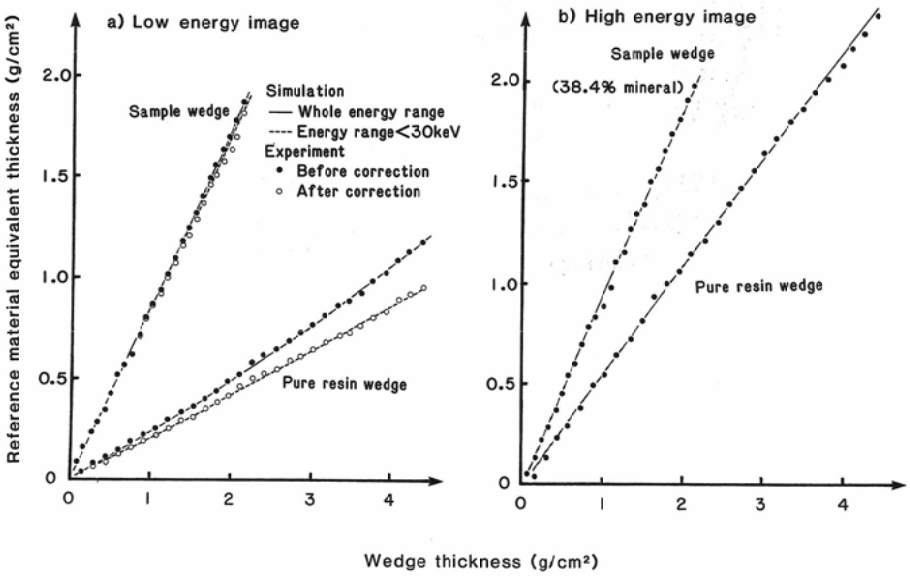

Fig. 9. The comparison of RMETs of the wedge phantoms measured by the experiment versus their thickness with that predicted by the simulation.
The measured RMETs (●) were very close to the simulated values (solid line). The RMETs after the correction for the higher energy x-ray contribution (○) were also very close to that predicted by the simulation (broken line). The agreement suggests that the corrections were accurate.

the predicted ones within the range of the experimental error by the film densitometry. The regression line through the points for the pure epoxy resin wedge in the back side film gave U_{ep}^*/U_r^* to be 0.545, which led U_b^*/U_{ep}^* to be 2.745. From Fig. 6, the tube potential was estimated to be 58.5 kV, which was close to 58.0 kV, the nominal setting value.

These agreement proved that the theoretical calculation by the mathematical model Eq. (9), using the spectral catalogue data by Birch et al. and photon cross section data by Storm et al. accurately simulated the actual image formation process of the experimental system using x-ray generator, phantoms, film-screen systems, which were manufactured independently from the calculation data.

Eq. (8) shows that the smaller Q*/Q led the higher precision of the correction for the high energy x-ray contribution to the tube side image. Fig. 8 indicats that the value of Q*/Q became larger for the higher tube potential and for the closer wave form to the constant potential. In the previous paper, I determined the standard tube potential to be 6-peak 55 kVp, at which Q*/Q was expected not to exceed 0.3 (Fig. 8), even the worst case of the setting error of the tube potential. In this experiment, the tube potential was 58 kV constant potential and a more larger Q*/Q was estimatd to be 0.32. The accuracy of the correction in the standard tube potential was assured by the fact that the high energy x-ray contribution was corrected accurately under this extremely unfavorable condition.

The correction terms for the sample phantom were smaller than that for the pure epoxy resin wedge having the same REMT. If the sample had the same composition as the reference wedge, RMET at the low energy would be the same as that at the high energy, and the correction term in Eq. (8) would be zero. The correction had, therefore, the more importance when the sample had the composition more different from

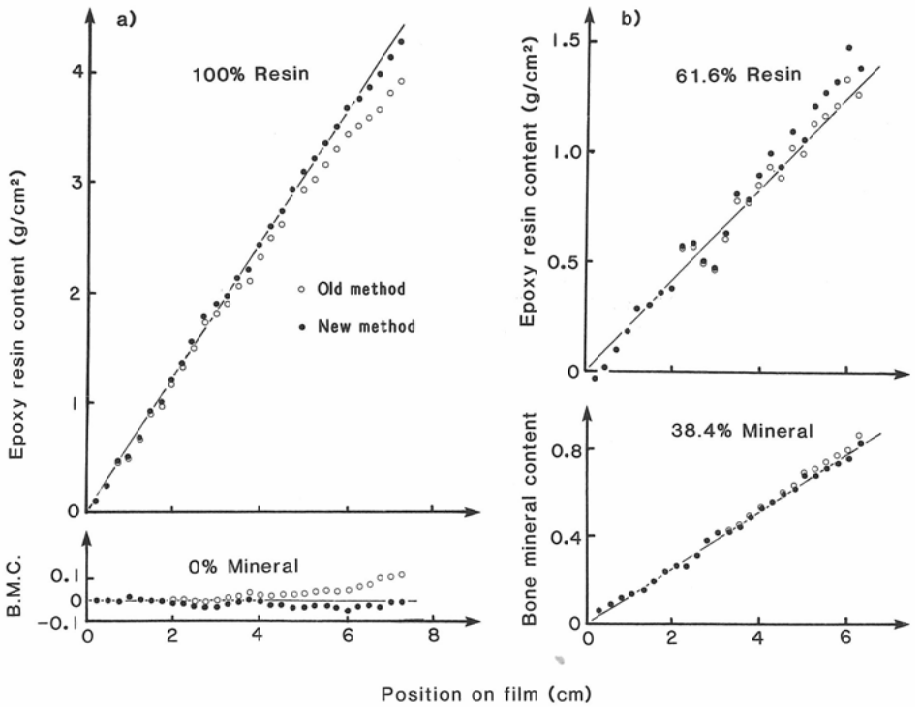

Fig. 10　The result of the dual-energy subtraction. a) Pure epoxy resin wedge b) Wedge shaped bone phantom containing 38.4% bone mineral equivalent material. The solid lines indicate the calculated values from the parameters listed in Tab. 2.
BMC; Bone mineral content

that of the reference wedge. In case the rough prediction of the bone mineral content in the sample was given, we had better chose the fraction of the bone mineral equivalent material in the reference wedge close to that of the sample for an accurate measurement.

Fig. 10 shows the results of the subtraction. The open circles indicate the results by the old method based on the first approximation. They were accurate only when the bone mineral content in the object was close to that of the reference wedge or the object was thin. The closed circles indicate the results by the new algorithm. They were accurate even when the object was thick and the bone mineral content in the object was different from that in the reference wedge.

5 Discussion

Because of the non-linear nature of white X-ray attenuation, the mathematical treatment of the dual energy image subtraction is not easy.

The simplest algorithm of energy subtraction is the weighted subtraction of the images. When the object consists of material A and B with thickness t_a and t_b, respectively, the gray level of each pixel in the subtraction image $F(t_a, t_b)$ is calculated by,

$$F(t_a, t_b)=\alpha\log(I_L)-\beta\log(I_H) \tag{16}$$
$$I_L=\int\Phi_L(E)dE$$
$$I_H=\int\Phi_H(E)dE$$

where Φ_L and Φ_H are energy fluence spectra of the transmitted x-rays at the two imaging plane of the tube side and the back side, respectively, and α and β are the weighting factors, respectively. As Arai[20] has explained, the image component of material A disappears when

$$\alpha/\beta=\mu_{aH}/\mu_{aL} \tag{17}$$

where μ_{aH} $\mu_{aL}$are the mean attenuation coefficient of material A, $\mu_a(E)$, weighted by the spectra Φ_H and Φ_L, respectively. The solutions of the simultaneous equations (1-1) and (1-2) can be transformed to the same expressions to the equations (16) and (17).

When the white x-rays are used, μ_{aH} and μ_{aL} vary independently with the object thickness. Material A, therefore, does not disappear in some other part of the image. When the dichromatic x-rays are used, the spectra are given by Dirac's delta functions.

$$\Phi_L(E)=q\delta(E_1)+q^*\delta(E_2) \qquad (q+q^*=I_L) \tag{18-1}$$
$$\Phi_H(E)=I_H\delta(E_2) \tag{18-2}$$

where q and q* denote the intensity of the low and the high energy component, which corespond to the first and the second term in the left side of the Eq. (7), respectively. μ_{aH} is constant equal to $\mu_a(E_2)$. μ_{aL} is calculated as,

$$\mu_{aL}=\{q\mu_a(E_1)+q^*\mu_a(E_2)\}/(q+q^*) \tag{19}$$

This value of μ_{aL} can be approximated by a constant when

$$q\mu_a(E_1)\gg q^*\mu_a(E_2) \tag{20}$$

This condition is realized for a wide range of the object thickness, when a K-dege filter is used. The results of the subtraction is, therefore, more accurate than that of white x-ray radiography.

The inequality (20) indicates the condition in which the weighted subtraction algorithm based on the first approximation is applicable. When it dose not hold, we must use an algoithm which takes into account of the non-linearity of the dichromatic x-ray attenuation. Lehmann et al.[21] showed that we could form two images of "basis materials" (for examples, aluminum and lucite, bone mineral and soft tissue) from dual energy images of any clinical object by solving non-linear simultaneous integral equations. We can solve the equations, however, only by the approximaiton if white x-rays are used. It requires long calculation time or a large scale computer system for the accurate approximation[22]. Because the dichromatic x-rays

were used instead of white x-rays in this work, the non-linear integral equaitons reduce to equations (8) and (3-2), whose exact solutions were easily calculated. The method which gives the exact solution is superior to the approximation method in the calculating speed and accuracy, and in the estimation of the reliability of the measured value.

The usage of K-edge filter has the disadvantage that the output x-ray intensity is reduced very much. In the recent years, however, the sensitivity of the image receptor and the load capacity of the x-ray generator are so improved that x-ray images can sufficiently be formed. The usage of the K-edge filter for the exact solution, I think, has a great advantage in total.

The beam hardening effect is the most important cause that reduces the accuracy of the quantitative image processing. The quantitative CT[25] is also realized using monochromatic beam. For the high intensity monochromatic source, the combination of the conventional x-ray tube and K-edge filter is very useful. Though the beam is not exact monochrome, we can regard it, from diagnostic view point, as monochrome because it is attenuated almost exponentially. The stability of the beam quality is a remarkable characteristic. The K-edge filters, I think, present the useful source for the quantitative x-ray diagnosis.

The method for simulating the image formation process in this work gives accuate results though it is simple. The computer program can be directly used for any other radiographing system not only film-screen system but also for the imaging plate radiography[13][14] and also for scanned projection radiography[12] when the atomic composition and thickness of the image receptor are known. Using this method, I thick, we can improve many systems of dual energy subtraction for the accurate quantification of the object thickness.

6 Conclusion

The image formation process in the dual-energy subtraction in a single exposure was theoretically analyzed. The objective radiographing system was such as;

The x-ray beam was dichromized by a tin filter.

The cassette contained two film-screen systems and a copper filter.

The reference wedge and the pure resin wedge were used to correct the fluctuation of the exposure factors and film processing condition and to estimate the tube potential.

The results of the analysis showed;

1) The back side image was formed by monochromatic x-rays. The beam quality varied with tube potential, but it could be estimated by the analysis of the wedge images.

2) The tube side image was formed by dichromatic x-rays. The photon energy of the low energy component was independent of the tube potential. The photon energy of the high energy component could be regarded as equal to that of the back side image.

3) The contribution of the high energy component to the tube side image depended on the object thickness, the tube potential and the filtration. This contribution could be analytically corrected based on the dichromatic x-ray attenuation model using the information on the tube potential and specifications of the imaging system.

4) Because the x-ray beam was dichromized and because dominant non-linear terms were included in the correction term, energy subtraction images were obtained as the exact solutions of linear simultaneous equations.

Using these results, a new dual energy subtraction algorithm was derived and the accuracy was improved for thick object whose bone mineral content was different from that in the reference wedge.

Nomenclature

Reference wedge

A wedge made of mixture of bone mineral equivalent material and epoxy resin put on the object plane together with the object to correct the fluctuation of the x-ray intensity, beam quality and the film processing condition.

RMET (Reference Material Equivalent Thickness)

The reference wedge thickness that presents the same gray level as that of the pixel of interest.

Symbols

E_1, E_2: Photon energy of x-rays producing the image ($E_1<E_2$).
U: Mass attenuation coefficient (cm^2/g)
X: Product of the density of the material and thickness (g/cm^2) in the object.
P: Weight fraction of the material in a mixture.
Q: Intensity fraction in the incident dichromatic x-rays.

Suffixes of U, X and P denote the relating material.

b: Bone mineral s: Soft tissue ep: Epoxy resin r: Reference wedge

Superfixes of U and Q denote relating photon energy

non: Photon energy E_1 *: Photon energy E_2

r: Mass attenuation coefficient ratio $U_b*/U_{ep}*$

Acknowledgments

I thank Professor Takehito Sasaki of Department of Radiology and Radiation Research, Faculty of Dentistry, Tokyo Medical and Dental University, for his discussion and reviweing the manuscript. My thanks are also extended to Professor Shigenobu Kanda and the late Associate Professor Keisuke Konishi of the Department of Radiology, Faculty of Dentistry, Kyushu University, who were willing to provide the facilities and gave useful suggestions on the x-ray spectroscopy. I also thank Associate Professor Yasuo Harata and Miss Rie Sakaino, for the checking my spectral catalogue data files.

The floppy disk files of photon cross sections[17] were provided by the Public Domain System of Study Group for Microcomputer Application to Dental Radiology (Office: Dept. of Radiology, Nippon Dental University, Tokyo).

This work was supported in part by Grant-in-Aid from the Ministry of Education, Science and Culture (59771509).

References

1) Kruger RA, Armstrong JD, Sorenson JA, et al: Dual energy subtraction technique for detecting calcification in solitary pulmonary nodules. Radiology 140: 213—219, 1981
2) Brody WR, Macovski A, Pelc NJ, et al: Intravenous arteriography using scanned projection radiography. Radiology 141: 509—514, 1981
3) Nishitani H, Umezu Y, Ogawa K, et al: Dual energy projection radiography using condenser x-ray generator and digital radiography apparatus. Radiology 161: 533—535, 1986
4) Nishitani H, Matsuura K: Dual-energy projection radiography using condenser discharge x-ray generator and FCR—determination of technical factors—Nippon Act. Radiol. 47: 644—650, 1987 (in Japanese)
5) Fraser RG, Hickey NM, Niklason LT, et al: Calcification in pulmonary nodules: Detection with dual-energy digital radiography. Radiology 160: 595—601, 1986
6) Takashima T: Single exposure energy subtraction chest radiography in the diagnosis of pulmonary cancer. Nippon Act. Radiol. 47: 455—464, 1987

7) Roos BO, Sköltborn H: Dual photon absorptiometry in lumber vertebrae. Acta Radiol. Ther. Phys. Biol. 13: 266—280, 1974
8) Witt RM, Mazess RB: Photon absorptiometry of soft tissue and fluid content: The method and its precision and accuracy. Phys. Med. Biol. 23: 620—629, 1978
9) Konishi K, Toyofuku F: Polychromatic photon absorptiometry. Nippon Act. Radiol. 40: 168—170, 1980 (in Japanese)
10) Katoh T, Chiba M, Kobayashi T: The basic study on bone mineral assessment with dual energy radiographic densitometry method. Dent. Radiol. 18: 278—295, 1978 (in Japanese)
11) Katoh T, Sakamaki K, Nakanura T: A new method for measurement of bone mineral deposition pattern. Bull. Tokyo Med. and Dent. Univ. 28: 91—98, 1981
12) Branes GT, Sones RA, Tesic MM, et al: Detector for dual-energy digital radiography. Radiology 156: 537—540, 1985
13) Hamakawa J, Tanaka R, Yoneda K: One shot dual energy subtraction of the chest using FCR system. Jpn. J. Radiol. Technol. 41: 1070—1076, 1985 (in Japanese)
14) Ishigaki T, Sakuma S, Horikawa Y, et al: One-shot dual-energy subtraction imaging. Radiology 161: 271—273, 1986
15) Okuyama T: A study of the quantitative analysis on the mineral contents of the bone by x-rays. Nippon Act. Radiol. 25: 755—790, 1965 (in Japanese)
16) Storm E, Israel HI: Photon cross sections from 1 keV to 100 MeV for elements Z=1 to Z=100. Nuclear Data Table A7: 565—681, 1970
17) Harata Y, Sakaino R, Shimura H: Data base for personal compuer: Attenuation coefficient and energy absorption coefficient of X and gamma ray. Dent. Radiol. 26: 257—263, 1986 (in Japanese)
18) Birch R, Marshal M, Ardran GM: Catalogue of spectral data for diagnostic x-rays. HPA Scientific Report Series 30: 1979
19) Kramers HA: On the theory of x-ray absorption and of the continuous x-ray spectrum. Phil. Mag. 46: 836, 1923
20) Arai T: Mathematical treatment of one-shot energy subtraction. Jpn. J. Radiol. Technol. 41: 1076—1078, 1985 (in Japanese)
21) Lehmann LA, Alvarez RE, Macovski A, et al: Generalized image combinaitons in dual kVp digital radiography. Med. Phys. 8: 659—667, 1981
22) Chuang KS, Huang HK: Comparison of four dual energy image decomposition methods. Phys. Med. Biol. 33: 455—466, 1988
23) Rüegsegger P, Anliker M, Dambacher M: Quantification of tabecular bone with low dose computed tomography. J. Comput. Assist. Tomogr. 5: 384—390, 1981